Geochemical Perspectives Letters

Expanding time-temperature chronometry for arc magmas with experimental MgO diffusion in hydrous melts

O. Callejas, M. Holycross, E. Gazel, E.G. Huggins

Supplementary Information

The Supplementary Information includes:

- Tables S-1 to S-18
- Analytical Techniques
- MgO Diffusivity Constraints
- Arrhenius Relationships
- Relationships between $\log_{10}D_{MgO}$ and Dissolved H_2O wt. %
- Supplementary Figures S-1 to S-4
- Supplementary Information References

Tables S-1 to S-18

Table S-1 Summary of experimental conditions and results.

Table S-2 Starting material compositions. Mix compositions normalised to major element composition of glass inclusion (AGR-19-02-03) from Agrigan, Marianas reported in Kelley and Cottrell (2012).

Table S-3 Arrhenius parameters (activation energy, E_a, and pre-exponential factor, D_0) for ~2.2 wt. % H_2O, ~4.5 wt. % H_2O, and Equation 4.

Table S-4 Electron probe (EPMA) standards used for the calibration of analyses (concentration gradients).

Table S-5 SCO3 concentration profiles at 1350 ºC and 1 GPa. Distance is in µm, oxides are in wt. %, locations of three distinct transects are provided by X, Y, Z coordinates.

Table S-6 SCO5 concentration profiles at 1350 ºC and 1 GPa. Distance is in µm, oxides are in wt. %, locations of three distinct transects are provided by X, Y, Z coordinates.

Table S-7 SCO8 concentration profiles at 1500 ºC and 1 GPa. Distance is in µm, oxides are in wt. %, locations of three distinct transects are provided by X, Y, Z coordinates.

Table S-8 SCO9 concentration profiles at 1550 ºC and 1 GPa. Distance is in µm, oxides are in wt. %, locations of three distinct transects are provided by X, Y, Z coordinates.

Table S-9 SCO10 concentration profiles at 1200 ºC and 1 GPa. Distance is in µm, oxides are in wt. %, locations of three distinct transects are provided by X, Y, Z coordinates.

Table S-10 SCO11 concentration profiles at 1125 ºC and 1 GPa. Distance is in µm, oxides are in wt. %, locations of three distinct transects are provided by X, Y, Z coordinates.

Table S-11 SCO12 concentration profiles at 1225 ºC and 1 GPa. Distance is in µm, oxides are in wt. %, locations of three distinct transects are provided by X, Y, Z coordinates.

Table S-12 SCO13 concentration profiles at 1175 ºC and 1 GPa. Distance is in µm, oxides are in wt. %, locations of three distinct transects are provided by X, Y, Z coordinates.

Table S-13 SCO14 concentration profiles at 1400 ºC and 1 GPa. Distance is in µm, oxides are in wt. %, locations of three distinct transects are provided by X, Y, Z coordinates.

Table S-14 SCO20 concentration profiles at 1225 ºC and 1 GPa. Distance is in µm, oxides are in wt. %, locations of three distinct transects are provided by BSE images.

Table S-15 SCO21 concentration profiles at 1125 ºC and 1 GPa. Distance is in µm, oxides are in wt. %, locations of three distinct transects are provided by BSE images.

Table S-16 SCO22 concentration profiles at 1200 ºC and 1 GPa. Distance is in µm, oxides are in wt. %, locations of three distinct transects are provided by BSE images.

Table S-17 SCO23 concentration profiles at 1175 ºC and 1 GPa. Distance is in µm, oxides are in wt. %, locations of three distinct transects are provided by BSE images.

Table S-18 SCO26 concentration profiles at 1225 ºC and 1 GPa. Distance is in µm, oxides are in wt. %, locations of three distinct transects are provided by BSE image.

Tables S-1 to S-4, and complete concentration gradients for individual experiments (Tables S-5 to S-18), are available for download (.xlsx) from the online version of this article at https://doi.org/10.7185/geochemlet.2541.

Analytical Techniques

Experimental Methods

All piston-cylinder experiments were conducted using the hot piston-in technique. All experiments utilized a two-step ramp: an initial rate of 300–400 °C/min to 50 °C lower than the target temperature, followed by a ramp of 30–50 °C/min to the final temperature. A temperature controller connected to a type-C thermocouple was used to monitor temperature (Table S-1). Each sample was maintained at the same pressure and selected temperature for the planned duration (Table S-1).

Ten of our reported fourteen experiments used a double capsule assembly of a graphite liner + exterior metal capsule with lower H^+ permeability. The graphite liner was used to buffer the experiment fO_2s at reducing conditions near the C-CO buffer (Ulmer and Luth, 1991) to allow direct comparison to the graphite-capsule experiments of Chen and Zhang (2008).

The choice of exterior metal capsule is guided by each material's permeability to H_2 and 1 atm melting point. For our low temperature (≤1225 °C) experiments, we used exterior $Au_{90}Pd_{10}$ capsules because, above the melting point of pure Au (>1064 °C), $Au_{90}Pd_{10}$ is most effective at retaining H_2O (Kawamoto and Hirose, 1994) (Fig. S-1). In two experiments (Table S-1), small volumes of Fe-oxide crystals formed in the melt due to use of single $Au_{90}Pd_{10}$ capsule assembly, which allowed for oxidation of the melt to occur. The presence of these crystals does not seem to affect MgO concentration gradients (see Tables S-11 and S-12), but their appearance is nonetheless undesirable. The addition of a graphite liner prohibits this phenomenon by buffering the melt at reducing conditions where oxidized iron phases do not form.

Our intermediate temperature (1450 > T > 1225 °C) experiments were conducted using exterior Ni metal (T_m = 1455 °C) capsules, following the methodology of Holycross and Watson (2018). Single graphite capsule assemblies were used in two experiments only because they were conducted at higher temperatures (≥1500 °C) above the melting point of metal. However, graphite is more permeable to H_2 diffusion (Luth, 1989) and water diffusion in silicate melt is fastest at high temperatures (Behrens *et al.*, 2004; Zhang and Stolper, 1991). Consequently, our highest temperature experiments experienced the greatest amount of water loss (Fig. S-1). Four experiments appeared to gain water, up to ~1 wt. % H_2O total compared to initial (Fig. S-1). It is not entirely clear why these experiments appeared to gain water while most experiments lost water. However, we note the experiments that gained water are generally colder and shorter compared to the experiments that lost water. The lower temperatures and shorter run times both act to limit the diffusive loss of H_2O through the capsule walls.

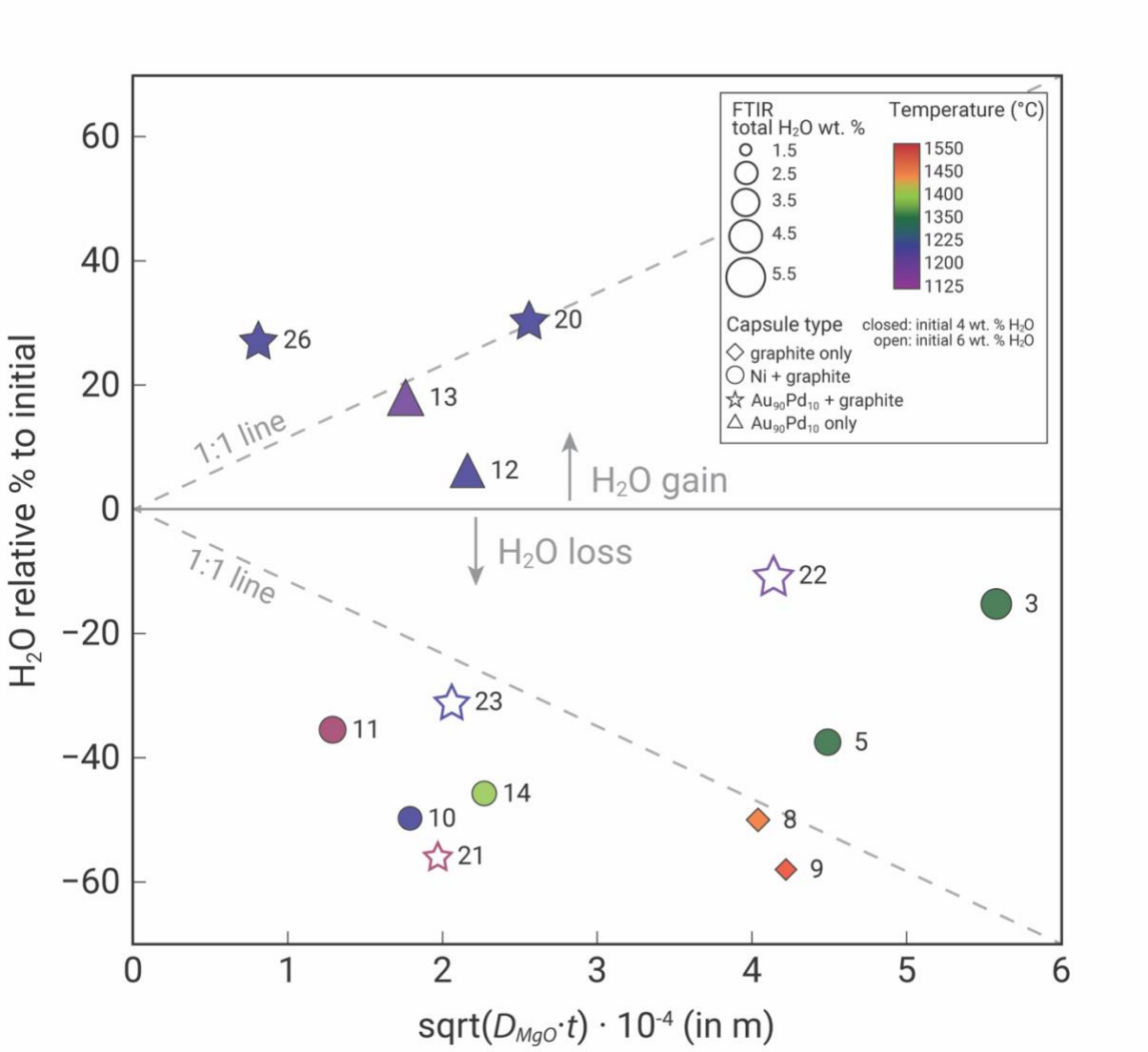

Figure S-1 H_2O content measured in each capsule type relative to initial (in %) as a function of sqrt($D_{MgO} \cdot t$). Marker size is dependent on final measured H_2O wt. % via FTIR. Colour gradient reflects temperature range conditions used in this study. Closed symbols show experiments with Mix 1 at initial 4 wt. % H_2O. Open symbols show experiments with Mix 2 at initial 6 wt. % H_2O. All experiments were run at 1 GPa. D_{MgO} values, duration of runs (t), and measured water contents are reported in Table S-1.

Data Collection via EPMA and SEM-EDS

Major and minor element compositions were measured for all experiments. Electron microprobe (EPMA) data collection was performed using a Cameca SXFive at Syracuse University for experiments SCO3 through SCO14. The following conditions were employed: 5 µm spot size, accelerating voltage of 15 kV, 10 nA beam current (increased to 20 nA for samples SCO12-14). The standards used for all data collection routines are reported in Table S-4. Additionally, back-scattered electron (BSE) images were obtained, and some examples are provided in Figure 1.

Major and minor element compositions were also measured for experiments SCO20-26. To do this, we used a JSM-IT700HR scanning electron microscope (SEM) and an Oxford Instruments ULTIM MAX energy dispersive x-ray spectrometer (EDS) at the Cornell Mass Spectrometry (CMaS) facilities in the Department of Earth and Atmospheric Sciences. The following conditions were employed: 10 µm spot size, accelerating voltage of 15 kV, 10 nA beam current. We used the Oxford Instruments Aztec software to characterize our chemical analyses. Total analytical time per data

point was set to 30–60 s and dead time on the order of 60 %. No standards were used during data collection. However, this does not affect our results nor conclusions because the concentration profiles of interest display the change in relative MgO concentration over distance. In this study, we focus on relative MgO wt. % across the experimental glass, so absolute concentrations do not necessarily have to be calibrated to obtain useful concentration profiles. But a normalisation still needs to be performed to represent proportional abundances of water content. Our SEM-EDS data sets were initially normalised to 100 %, using the Oxford Instruments Aztec software. Then, we scaled all major and minor element compositions in each sample so the totals would add up to 96 wt. % or 94 wt. % for an initial 4 or 6 wt. % H_2O, respectively. When comparing our SEM-EDS data to the previously obtained EPMA data, we notice general agreement between our measurements. Except for Na wt. % values as these were lower than those obtained via EPMA. This is not uncommon since the presence of water can promote Na loss and electron beam can impose damage on the sample, which results in artificially low values (Kuehn *et al.*, 2011). Again, since we are particularly interested in MgO wt. %, we can neglect the uncertainty in abundance of Na.

FTIR Conditions and Constraints

Spectra were collected on a Thermo Nicolet iN10MX FTIR by scanning from 1200 cm^{-1} to 5500 cm^{-1} at high resolution (256 scans), 150x150 µm aperture, using a CaF_2 beamsplitter and a liquid nitrogen-cooled MCT-A detector. A minimum of three scans were taken in each glass sample to determine homogeneity in volatile concentrations. The Thermo-Nicolet OMNIC Picta software was used to collect spectra and reduce noise. We performed background subtraction by using the Fityk software and setting a cubic spline baseline on each spectrum, following the methods outlined in Dixon *et al.* (1995). Then, peak fitting was performed using 3–4 Gaussian functions. Total water content was calculated using the amplitude of the total H_2O peak at 3530 cm^{-1}. The molar absorptivity coefficient (ε) used at this wavenumber was 63 $L \cdot mol^{-1} \cdot cm^{-1}$ as determined by Dixon *et al.* (1995). When the 3530 cm^{-1} peak was oversaturated, we used the amplitudes of the OH^- + H_2O_m peaks at 4500 cm^{-1} and 1630 cm^{-1}, respectively. The ε for each corresponding wavenumber was calculated by using the equation fit data defined in Dixon *et al.* (1995):

$$\varepsilon^{4500} = -2 \cdot 3 + 4.4 \cdot T \quad \text{(S-1)}$$

$$\varepsilon^{1630} = -66.3 + 141.7 \cdot T \quad \text{(S-2)}$$

where T is (Si + Al)/total cations.

The thickness of each sample was measured using a petrographic microscope. These measurements were used to calibrate the average H_2O contents across samples, thus minimizing variations in the absorption spectra and increasing accuracy. Error bars were determined by calculating a range of total H_2O content based on the smallest and largest thickness measurements within a given sample. The final total H_2O contents are reported as the average of each sample in Table S-1 and Figure S-4.

MgO Diffusivity Constraints

We conducted an experiment time-series at T = 1225 °C, P = 1 GPa, and three different times (Table S-1) to ensure our MgO diffusivities were independent of time. A time series may also help to constrain the inherent uncertainty of our experiments by testing whether we can obtain the same result multiple times. In this way, a times series can also be used to determine the precision of our MgO diffusion coefficients. Each D_{MgO} was calculated using Equation 1. The results were then used to ascertain errors by a conventional sample standard deviation formula,

$$\sigma = \sqrt{\frac{\sum(x_i - \bar{x})^2}{N - 1}} \quad \text{(S-3)}$$

where x_i is a given value (*i.e.* $\log_{10}D_{MgO}$), $\bar{x}$ is the average obtained from the experiments in the time-series (*i.e.* SCO12, 20, 26), $N = 3$ (sample size), and σ is the calculated error. We document our diffusion coefficient values as $\log_{10}D_{MgO}$ (Table S-1; Fig. 3), so the associated errors are reported as ±0.1 logarithmic units (Table S-1; Fig. S-2), under the assumption that our time-series sample population accurately reflects the inherent variability in all experiments conducted for this study. This error is comparable to the standard error (up to ±0.1 log unit) of the fit reported by the ORIGIN™ software used to extract D_{MgO} values via semi-infinite solution (Table S-1). ORIGIN™ uses statistical analysis to evaluate the quality of an error function solution fit to data points.

The time-series experiments all used mix 1, which initially contained 4 wt. % H_2O. We observe a slight increase in D_{MgO} in the most hydrous experiment in the time series. SCO20 contained 5.22 wt. % H_2O at the end of the experiment and records the fastest value of D_{MgO}. This is consistent with our interpretation that our calculated D_{MgO} values reflect the final measured concentration of H_2O in the glass, rather than the initial amount. In the latter case, we would expect all time-series D_{MgO} to be the same, but that is not the case. Instead, we observe dependence on final measured H_2O content in the glass.

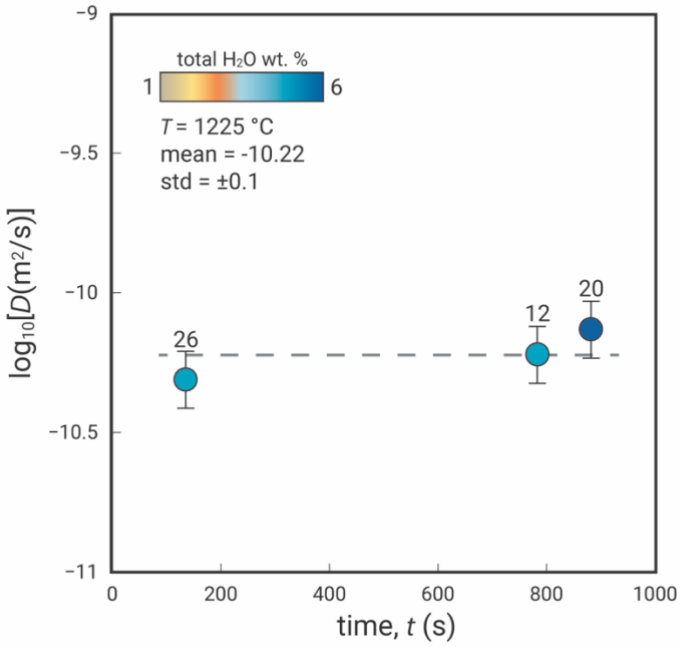

Figure S-2 Time-series piston-cylinder experiments at 1225 °C and 1 GPa. All $\log_{10}D_{MgO}$ were calculated using Equation 1. Error bars are shown and were calculated using Equation S-3. Measured water contents are depicted by colour gradient and specific values are documented in Table S-1. Grey dashed line is plotted as the calculated mean ($\bar{x}$) to demonstrate the extent of variability among experiments conducted at the same *P*-*T* conditions.

Arrhenius Relationships

Our piston-cylinder experiments had initial contents of ~4 and ~6 wt. % water (Table S-2). However, we reported variable water compositions (Table S-1) and grouped the data as two different Arrhenius relationships based on the final measured water contents. If we were to arrange these two populations by initial water contents, the dependence for each trend would be less consistent (Fig. S-3). For instance, in the case of the initial 4 wt. % dissolved H_2O (pink, dashed

line), the strength of the correlation decreased ($r^2 = 0.94$) and at least three experiments fall out of the error range (i.e., the error bars no longer overlap with the Arrhenius line). In the case of the initial 6 wt. % dissolved H_2O (purple, dashed line), the strength of the correlation increased ($r^2 = 0.93$). However, the trend is only constrained by three data points, and it is limited to the lowest *T*s (1125–1200 °C). Extrapolating this Arrhenius line to higher *T*s will result in an overlap with at least three experiments from the initial 4 wt. % water group.

As noted in Figure 3, the first Arrhenius relation (shown in orange, at average 2.2 wt. % H_2O, $r^2 = 0.99$) can be fit by a linear regression such that,

$$\ln D_{MgO} = \ln D_0 - \frac{E_a}{RT} \quad \text{(S-4)}$$

where the pre-exponential factor (D_0) is calculated to be 4.04E-05 ± 1.48E-05 m^2/s and the activation energy (E_a) is 173,255 ± 4,891 J/mol (also reported in Table S-3 for more direct accessibility). The second Arrhenius relation (shown in blue, at average 4.5 wt.% H_2O, $r^2 = 0.88$) can also be fit by Equation S-4, and it yields the following parameters: D_0 = 7.26E-06 ± 5.51E-06 m^2/s and E_a = 143,977 ± 21,681 J/mol (Table S-3). Chen and Zhang (2008) documented their values as D_0 = 3.73E-04 m^2/s and E_a = 218,000 J/mol. In comparison, the presence of ~2.2 wt. % dissolved water in the silicate melt already decreases the E_a by about 20 %. The presence of ~4.5 wt. % dissolved water further decreases the E_a by about 33 %. This is in alignment with the expected inverse relationship: as dissolved water increases, activation energy decreases.

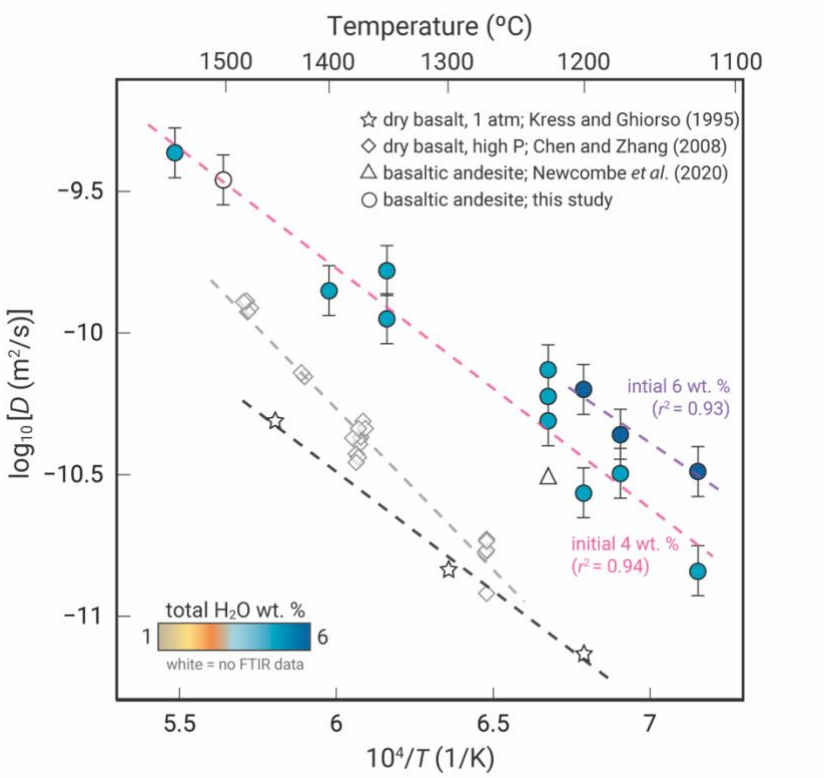

Figure S-3 D_{MgO} as a function of *T* showing Arrhenius relationships at initial 4 and 6 wt. % water for our successful experiments, compared to D_{MgO} in dry basalt at 1 atm (Kress and Ghiorso, 1995), dry MORB at 0.47–1.42 GPa (Chen and Zhang, 2008), and a hydrous D_{MgO} data point (Newcombe *et al.*, 2020). Colour gradient shows initial water added to the experiment.

Relationships between $log_{10}D_{MgO}$ and Dissolved H_2O wt. %

To understand how $log_{10}D_{MgO}$ changes as a function of dissolved water, we conducted piston-cylinder experiments at either initial 4 wt. % or 6 wt. % dissolved water and at constant T, P (Fig. S-4). We used the Arrhenius parameters published in (Chen and Zhang, 2008) to calculate D_{MgO} in dry MORB at a given T to extend our observations to ~0 wt. % dissolved H_2O. The observed trends displayed a linear relationship ($r^2 \geq 0.92$). We note that there is one water series experiment at 1200 °C where the relationship between dissolved H_2O content and D_{MgO} may be better fit by an asymptotic or square-root fit rather than a linear regression. However, because our other three water-series experiments are best fit by a linear regression, we applied the same fit to the 1200 °C data to maintain internal consistency.

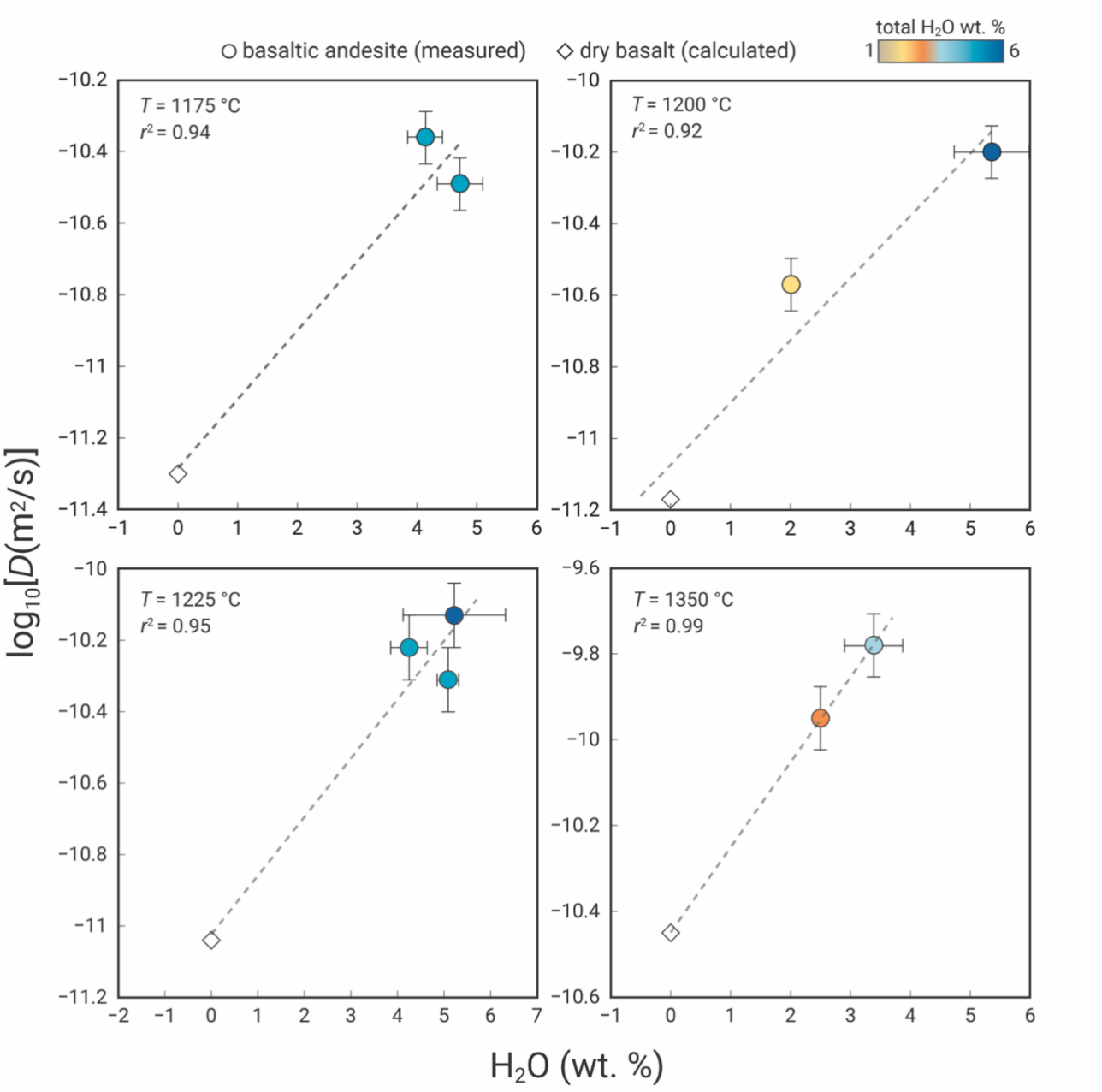

Figure S-4 Linear relationships between $log_{10}D_{MgO}$ and dissolved H_2O contents. Each panel shows calculated dry MgO diffusivities from Chen and Zhang (2008) at a given T and measured MgO diffusivities in hydrous melts (this study). All experiments were run at 1 GPa.

Supplementary Information References

Behrens, H., Zhang, Y., Xu, Z. (2004) H_2O diffusion in dacitic and andesitic melts. *Geochimica et Cosmochimica Acta* 68, 5139–5150. https://doi.org/10.1016/j.gca.2004.07.008

Chen, Y., Zhang, Y. (2008) Olivine dissolution in basaltic melt. *Geochimica et Cosmochimica Acta* 72, 4756–4777. https://doi.org/10.1016/j.gca.2008.07.014

Dixon, J.E., Stolper, E.M., Holloway, J.R. (1995) An Experimental Study of Water and Carbon Dioxide Solubilities in Mid-Ocean Ridge Basaltic Liquids. Part I: Calibration and Solubility Models. *Journal of Petrology* 36, 1607–1631. https://doi.org/10.1093/oxfordjournals.petrology.a037267

Holycross, M.E., Watson, E.B. (2018) Trace element diffusion and kinetic fractionation in wet rhyolitic melt. *Geochimica et Cosmochimica Acta* 232, 14–29. https://doi.org/10.1016/j.gca.2018.04.006

Kawamoto, T., Hirose, K. (1994) Au-Pd sample containers for melting experiments on iron and water bearing systems. *European Journal of Mineralogy* 6, 381–386. https://doi.org/10.1127/ejm/6/3/0381

Kelley, K.A., Cottrell, E. (2012) The influence of magmatic differentiation on the oxidation state of Fe in a basaltic arc magma. *Earth and Planetary Science Letters* 329, 109–121. https://doi.org/10.1016/j.epsl.2012.02.010

Kress, V.C., Ghiorso, M.S. (1995) Multicomponent diffusion in basaltic melts. *Geochimica et Cosmochimica Acta* 59, 313–324. https://doi.org/10.1016/0016-7037(94)00286-U

Kuehn, S.C., Froese, D.G., Shane, P.A.R., INTAV Intercomparison Participants (2011) The INTAV intercomparison of electron-beam microanalysis of glass by tephrochronology laboratories: Results and recommendations. *Quaternary International* 246, 19–47. https://doi.org/10.1016/j.quaint.2011.08.022

Luth, R.W. (1989) Natural versus experimental control of oxidation state: Effects on the composition and speciation of C-O-H fluids. *American Mineralogist* 74, 50–57. http://www.minsocam.org/ammin/AM74/AM74_50.pdf

Newcombe, M.E., Plank, T., Zhang, Y., Holycross, M., Barth, A., Lloyd, A.S., Ferguson, D., Houghton, B.F., Hauri, E. (2020) Magma Pressure-Temperature-Time Paths During Mafic Explosive Eruptions. *Frontiers in Earth Science* 8, 531911. https://doi.org/10.3389/feart.2020.531911

Ulmer, P., Luth, R.W. (1991) The graphite-COH fluid equilibrium in P, T, fO_2 space: An experimental determination to 30 kbar and 1600° C. *Contributions to Mineralogy and Petrology* 106, 265–272. https://doi.org/10.1007/BF00324556

Zhang, Y., Stolper, E.M. (1991) Water diffusion in a basaltic melt. *Nature* 351, 306–309. https://doi.org/10.1038/351306a0